JOURNAL OF GEOPHYSICAL RESEARCH, VOL. 108, NO. B6, 2288, doi:10.1029/2002JB002161, 2003

# Stress field in the subducting lithosphere and comparison with deep earthquakes in Tonga

A. Guest[1] and G. Schubert[2]
Department of Earth and Space Sciences, University of California, Los Angeles, California, USA

C. W. Gable
Earth and Environmental Sciences Division, Los Alamos National Laboratory, Los Alamos, New Mexico, USA

Received 20 August 2002; revised 24 January 2003; accepted 27 February 2003; published 6 June 2003.

[1] We present a numerical model of the subducting lithosphere that provides an alternative explanation for stresses causing deep earthquakes. Our model lithosphere is composed of $\alpha$ olivine, $\beta$ spinel, $\gamma$ spinel, and perovskite + magnesiowüstite. The heat conduction equation is solved to determine temperature conditions in the slab and to locate the equilibrium phase transformations in pressure-temperature space. Volumetric strains in the subducting lithosphere are calculated from the density of individual phases and from the heat released or consumed in the phase changes. These strains are used as sources of stress in the subducting lithosphere. Dislocation creep and Peierls stress creep laws are included in the viscoelastic rheology. Volumetric reductions due to equilibrium phase transformations cause high shear stress in the transition zone because of the variable viscosity inside the subducting slab. Aspects of the model shear stresses are in agreement with observations of high seismic activity in the Tonga-Wadati Benioff zone. Compression is oriented along the dip of the slab, and extension is oriented in the plane perpendicular to the compression axis. Since our model stresses agree with the seismic observations, and because the model stresses are larger than those caused by buoyancy forces, our model provides a possible explanation of stresses causing deep earthquakes. Also, our model does not need metastability of olivine to explain the occurrence of high shear stress in the transition zone. *INDEX TERMS:* 8120 Tectonophysics: Dynamics of lithosphere and mantle—general; 8149 Tectonophysics: Planetary tectonics (5475); 8164 Tectonophysics: Stresses—crust and lithosphere; *KEYWORDS:* stress, subduction, Tonga, phase transformations, viscoelastic rheology, numerical modeling

**Citation:** Guest, A., G. Schubert, and C. W. Gable, Stress field in the subducting lithosphere and comparison with deep earthquakes in Tonga, *J. Geophys. Res.*, *108*(B6), 2288, doi:10.1029/2002JB002161, 2003.

## 1. Introduction

[2] The state of stress is important for understanding the fate of subducting slabs and the dynamics of mantle convection. The distribution of stresses in the subducting lithosphere is determined by the distribution of the sources of stress and by the strength of the lithosphere that enables these stresses to persist. Temperature and pressure effects on subducting minerals are one of the major sources of stress and one of the factors controlling the state of stress. The densities of minerals change during subduction due to increasing temperature and pressure, and buoyancy forces arise. As minerals undergo phase transformation, latent heat is released or consumed and internal stresses occur due to the change of volume. The viscosity of the lithosphere is responsible for relaxation of the stresses; viscosity decreases with temperature and magnitude of shear stress and increases with pressure. Other pressure-dependent and temperature-dependent factors, such as volatile content and mineral grain size, influence viscosity [e.g., *Karato*, 1997; *Karato et al.*, 2001] and thus influence the state of stress in the subducting lithosphere.

[3] The complex behavior of the subducting lithosphere is difficult to model, partly because of the uncertainties in relevant parameter values and partly because of numerical challenges. Several numerical models of stress with different simplifications have been studied: models including only buoyancy forces [*Goto et al.*, 1985, 1987; *Bina*, 1996; *Yoshioka et al.*, 1997]; models including thermal stresses and volumetric reduction stresses [*Goto et al.*, 1983, 1987; *Devaux et al.*, 2000]; models including only the $\alpha$ olivine to $\beta$ spinel phase transformation [*Goto et al.*, 1987; *Devaux et al.*, 1997, 2000]; and models including all phase transformations of olivine [*Bina*, 1996; *Yoshioka et al.*, 1997]. These models showed that downdip compression generally observed in subduction zones can be explained by buoyancy forces resulting from a density contrast between the subducting lithosphere and the ambient mantle due to

[1] Also at Geophysical Institute, Praha, Czech Republic.
[2] Also at Institute of Geophysics and Planetary Physics, University of California, Los Angeles, California, USA.


0148-0227/03/2002JB002161$09.00

elevated or depressed phase boundaries [e.g., *Goto et al.*, 1985; *Bina*, 1996; *Yoshioka et al.*, 1997; *Devaux et al.*, 2000] or by stresses due to volumetric reduction of the metastable $\alpha$ olivine during phase transformation [*Goto et al.*, 1987; *Devaux et al.*, 2000]. The latter stresses have higher magnitude and are thus a more probable explanation of deep earthquakes [*Devaux et al.*, 2000]. The stresses due to the volume changes of equilibrium phase transformations have not been studied sufficiently. *Goto et al.* [1987] studied the effects of the equilibrium $\alpha$ olivine to $\beta$ spinel phase transition and found downdip tension in the central part of the subducting slab at depths of the transition zone. However, the kinetic data they used are no longer relevant.

[4] Our stress calculations focus on the effects of volume changes in the entire sequence of olivine phase transformations: $\alpha \rightarrow \beta \rightarrow \gamma \rightarrow$ perovskite + magnesiowüstite. We consider equilibrium phase transformation for all phase changes. We use a viscoelastic rheology dependent on temperature, pressure, shear stress, and Peierls stress, that is, the dislocation creep and the Peierls stress creep laws. We simulate diffusion creep (grain size-sensitive rheological law) by including a low-viscosity layer below phase boundaries. We also vary the mantle temperature profile and some rheological parameters (e.g., the magnitude of Peierls stress) in order to study their effects on shear stress magnitude. Since we consider the slab as a two-dimensional structure, we study the effect of the boundary condition in the trench-parallel direction by comparing stress solutions for plane strain and plane stress boundary conditions. Finally, we compare our model with seismic activity at the Tonga subduction zone and discuss the relevance of our model to this example.

[5] The plan for this paper is as follows. The model is described in section 2 together with model input parameters. Numerical results are presented in section 3. Then, the model is compared to seismic observations in the Tonga subduction zone in section 4. Section 5 discusses the most important results. A summary is given in section 6.

## 2. Model Description

### 2.1. Geometry

[6] The subducting plate is considered as a two-dimensional structure. The slab descends into the mantle with a velocity $v$ at an angle $\delta$ to the horizontal (Figure 1). In our model, $v = 10$ cm yr$^{-1}$ and $\delta = 50°$. The thickness of the lithosphere $De$ is determined by the age of the lithosphere at the onset of subduction. We consider $De = 95$ km, corresponding to an age older than 70 Myr [*Stein and Stein*, 1992].

### 2.2. Momentum and Rheological Equations

[7] The balance of forces is expressed by the equation

$$\frac{\partial \sigma_{ij}}{\partial x_i} + f_i = 0, \qquad i = 1,2,3 \quad j = 1,2,3 \tag{1}$$

where $\sigma_{ij}$ is the stress tensor and $f_i$ is the sum of the body forces acting on the slab. The $x_i$ are the Cartesian coordinates described in Figure 1. The stress $\sigma_{ij}$ does not include the hydrostatic pressure of the surrounding mantle. The body forces $f_i$ thus include the buoyancy forces due to the difference of density between a given point inside the slab and a point at the same depth far from the slab. In our calculations we put $f_i = 0$ because we assume that the gravitational torque applied to the slab is balanced by the lifting pressure torque [*Turcotte and Schubert*, 1982]. This balance sets the constant dip of the lithosphere. When the dip of the lithosphere remains constant, the stress due to buoyancy forces is at least 1 order of magnitude less than the stresses due to phase change-induced volumetric changes [*Devaux et al.*, 2000].

[8] We use the constitutive relation of a Maxwell body to describe the viscoelastic behavior:

$$\dot{\sigma}_{ij} + \frac{\mu}{\nu}\left(\sigma_{ij} - \frac{1}{3}\sigma_{kk}\delta_{ij}\right) = K\dot{\epsilon}_{kk}\delta_{ij} \qquad i = 1,2,3 \quad j = 1,2,3$$
$$+2\mu\left(\dot{\epsilon}_{ij} - \frac{1}{3}\dot{\epsilon}_{kk}\delta_{ij}\right) - K\dot{\epsilon}^T_{ij}\delta_{ij} - K\dot{\epsilon}^V_{ij}\delta_{ij}, \qquad k = 1,2,3 \tag{2}$$

where $\dot{\epsilon}_{ij}$ is the time derivative of the strain tensor $\epsilon_{ij}$:

$$\epsilon_{ij} = \frac{1}{2}\left(\frac{\partial u_i}{\partial x_j} + \frac{\partial u_j}{\partial x_i}\right) \tag{3}$$

and where $u_i$ is the displacement of a point at time $t$ from its initial position in our reference frame, $K$ is the bulk modulus, $\mu$ is the shear modulus, $\nu$ is the viscosity, and $\delta_{ij}$ is the Kronecker delta. The variables $\dot{\epsilon}^T_{ij}$ and $\dot{\epsilon}^V_{ij}$ are the strain rates inside the slab due to thermal expansion from the warming of the slab and volume contraction due to phase transformations:

$$\dot{\epsilon}^T_{ij} = \frac{1}{3}\alpha\delta_{ij}\dot{T} \tag{4}$$

$$\dot{\epsilon}^V_{ij} = -\frac{1}{3}\left(\frac{\dot{\rho}}{\Delta\rho}\right)\delta_{ij}. \tag{5}$$

In equation (4), $\alpha$ is the coefficient of thermal expansion and $\dot{T}$ is the time derivative of the temperature. In equation (5), $\rho$ is density, $\Delta\rho$ is the positive density difference between the high-pressure phase and the low-pressure phase, and $\dot{\rho}/\Delta\rho$ is the time derivative of the fractional volume change of a phase transformation. Parameter values are listed in Tables 1 and 2 and are discussed in detail in sections 2.8, 2.9, and 2.10. The thermal expansion term in equation (4) causes stresses when it is distributed nonuniformly inside the slab, that is, when the time rate of change of temperature is spatially nonuniform. The volumetric reduction term given by equation (5) has similar effects (only opposite in sign). Note that these terms are not dependent on the gravitational field.

### 2.3. Boundary Conditions

[9] The boundary conditions on the bottom ($x_1 = 0$), on the top ($x_1 = De$), and on the leading edge ($x_2 = 0$) of the

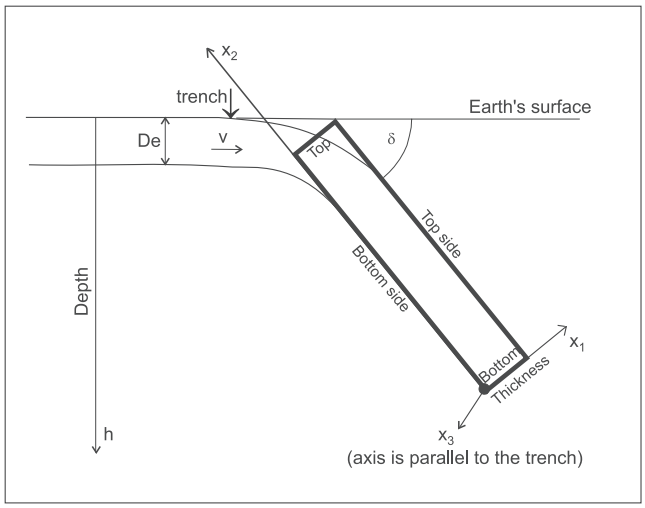


**Figure 1.** Sketch of the slab model.

slab are chosen to be stress free so that only the pressure in the mantle acts on these boundaries. The slab is pinned ($u_i$ = 0) at the trench. We tested both zero displacement ($u_3$ = 0, plane strain) and zero stress ($\sigma_{33}$ = 0, plane stress) boundary conditions in the direction parallel to the trench axis.

### 2.4. Numerical Analysis

[10] Equations (1)–(5) applied to a two-dimensional structure form a system of two coupled equations with unknowns $u_1$ and $u_2$. The equations are solved using a staggered-grid finite difference technique [*Madariaga*, 1976] with staggered $u_1$ and $u_2$ variables. We use a 2-km grid spacing in the $x_1$ and $x_2$ directions. The numerical code was tested against analytic solutions of several problems (elastic deformation of a slab by its own weight; elastic deformation of a slab under tension; viscoelastic deformation of a uniformly loaded slab supported on one side). We also performed a number of numerical tests for cases with

**Table 1.** Elastic and Creep Parameters

| Parameters | α | β | γ | *pv* | *Mg*0 |
|---|---|---|---|---|---|
| Molar volume ($V_m$), cm$^3$ mol$^{-1}$ | 43.67 | 40.52 | 39.66 | 24.46 | 11.25 |
| Density ($\rho_0$), kg m$^{-3}$ | 3222[a] | 3473[a] | 3548[a] | 4104[b] | 3583[b] |
| Bulk modulus ($K$), GPa | 129[c] | 174[c] | 184[c] | 261[d] | 164[e] |
| Pressure derivative of bulk modulus ($(\partial K/\partial p)_T$) | 5.2[c] | 4.3[d] | 4.1[d] | 4.0[d] | 4.2[e] |
| Shear modulus (μ), GPa | 82[e] | 114[f] | 119[g] | 184[h] | 132[e] |
| Pressure derivative of shear modulus ($(\partial\mu/\partial p)_T$) | 1.4[i] | 1.4[i] | 1.8[b] | 2.0[b] | 2.5[e] |
| Temperature derivative of shear modulus ($(\partial\mu/\partial T)_p$), GPa K$^{-1}$ | −0.013[e] | −0.014[b] | −0.014[b] | −0.028[b] | −0.024[e] |
| Thermal expansivity (α), $10^{-5}$ K$^{-1}$ | 3.05[j] | 2.71[j] | 2.37[j] | 1.73[d] | 3.12[e] |
| Grüneisen parameter (γ) | 1.25[c] | 1.30[c] | 1.35[c] | 1.96[k] | 1.54[e] |
| Power ($n$) for dislocation creep | 3.5[m] | 3.5[n] | 3.5[m] | 3.0[o] | 3.3[p] |
| Preexponential coefficient for dislocation creep ($C_1$), Pa$^{-n}$ s$^{-1}$ | $\frac{3.5\cdot10^{22}}{\mu^n(p,T)}$[m] | $\frac{4.0\cdot10^{22}}{\mu^n(p,T)}$[n] | $\frac{4.0\cdot10^{22}}{\mu^n(p,T)}$[m] | $2.1186\times10^{9}$[o] | $\frac{10^{24}}{1.381T}b\mu(p,T)^{(1-n)}$[p,q] |
| Preexponential coefficient for Peirls's law ($C_2$), $10^{11}$ s$^{-1}$ | 5.7[l] | 7.0[n] | 7.0[m] | | |
| Peirl's stress ($\sigma_P$), GPa | 8.5[l] | 10[n] | 10[m] | | |
| Constant ($g_m$) proportional to activation energy | 31[m] | 31[n] | 31[m] | 20.8[o] | 10.3[p] |
| Pressure dependence of melting temperature ($T_m(p)$), K | $2171(1+\frac{p}{2.44})^{\frac{1}{11.4}}$[r,s] | $46.38p + 1833.15$[t] | $46.38p + 1833.15$[t] | $26.695p + 2572.5$[u] | $-0.539p^2 + 52.15p + 3043.63$[v] |

[a]From *Jeanloz and Thompson* [1983].
[b]From *Duffy and Anderson* [1989].
[c]From *Akaogi et al.* [1987].
[d]From *Yusa et al.* [1993].
[e]From *Anderson and Isaak* [1995].
[f]From *Sawamoto et al.* [1984].
[g]From *Weidner et al.* [1984].
[h]From *Yeganeh-Haeri et al.* [1989].
[i]From *Isaak et al.* [1989].
[j]From *Akaogi et al.* [1989].
[k]From *Stixrude et al.* [1992].
[l]From *Goetze and Evans* [1979].
[m]From *Karato et al.* [2001].
[n]Assumed to be the same as for γ.
[o]From *Wright et al.* [1992].
[p]From *Frost and Ashby* [1982].
[q]Where $b = 2.98\times10^{-10}\exp(p/3K_0)$.
[r]From *Presnall and Walter* [1993].
[s]Where $p$ is pressure (GPa).
[t]The variable $T_m(p)$ is linearly interpolated between two points: (1) $T_m(p)$ of α olivine at pressure of α to β reaction; and (2) $T_m(p)$ of perovskite at pressure of γ to *pv* + *MgO* reaction.
[u]From *Wang* [1999].
[v]From *Zerr and Boehler* [1994].

**Table 2.** Model Parameters

| Name | Value |
|---|---|
| Velocity ($v$), mm yr$^{-1}$ | 100 |
| Dip angle ($\delta$), deg | 50 |
| Gravity acceleration ($g$), m s$^{-2}$ | 9.8 |
| Thickness of lithosphere ($De$), km | 95 |
| Temperature at base of lithosphere ($T_l$), K | |
| Cold[a] | 1473 |
| Hot[a] | 1723 |
| Adiabatic gradient in mantle,[b] K km$^{-1}$ | 0.3 |
| Slab density ($\rho$),[b] kg m$^{-3}$ | 3300 |
| Specific heat ($c_p$),[c] J kg$^{-1}$ K$^{-1}$ | $1.05 \times 10^{-5}$ |
| Thermal conductivity ($k$),[b] W m$^{-1}$ K$^{-1}$ | 3.465 |
| First-order thermal expansivity ($\alpha_0$),[b] K$^{-1}$ | $3 \times 10^{-5}$ |
| Second-order thermal expansivity ($\alpha_1$),[b] K$^{-1}$ m$^{-1}$ | $2 \times 10^{-11}$ |

[a]From *Stein and Stein* [1992].
[b]From *Turcotte and Schubert* [1982].
[c]From *Devaux et al.* [1997].

spatially dependent physical parameters and compared them against the numerical results of *Devaux et al.* [2000].

### 2.5. Temperature

[11] In order to solve for the stress distribution in the slab, we first determined the temperature, the mineralogical composition, and the values of elastic parameters and density in the temperature-pressure space of the subducting slab. The values are calculated separately and then are used as input for equations (1)–(5). The appropriate equations are described in this section and in sections 2.6, 2.7, 2.8, 2.9, and 2.10.

[12] The temperature distribution inside the slab is computed using the heat conduction equation

$$\rho c_p \frac{\partial T}{\partial t} = k\left(\frac{\partial^2 T}{\partial x_1^2} + \frac{\partial^2 T}{\partial x_2^2}\right) + \rho v \alpha g T \sin\delta + Q_L, \qquad (6)$$

in which adiabatic heating (second term on the right side) and latent heat $Q_L$ released or absorbed during phase transformations of minerals are included. The specific heat at constant pressure is $c_p$, $t$ is the time, and $k$ is the thermal conductivity. The coefficient of volume expansion $\alpha$ is assumed to be only a function of the depth $h$:

$$\alpha = \alpha_0 - \alpha_1 h. \qquad (7)$$

[13] The adiabatic temperature profile in the mantle is used as a boundary condition on the temperature in the slab, and the distribution of temperature in the oceanic lithosphere before subduction is used as an initial condition (Figure 2 and Table 2):

$$T(x_1, t=0) = (T_l - 273\text{K})\left(1 - \frac{x_1}{De}\right) + 273\text{K}, \qquad (8)$$

where $T_l$ is the temperature at the base of lithosphere at the onset of subduction. The shear heating term [e.g., *Schubert et al.*, 1976] was not included in the calculations, although frictional dissipation could be important in the slab [*Cherukuri and Shawki*, 1995; *Larsen and Yuen*, 1997; *Kameyama et al.*, 1999; *Regenauer-Lieb and Yuen*, 2000]. With the neglect of shear heating, the heat equation (6) and

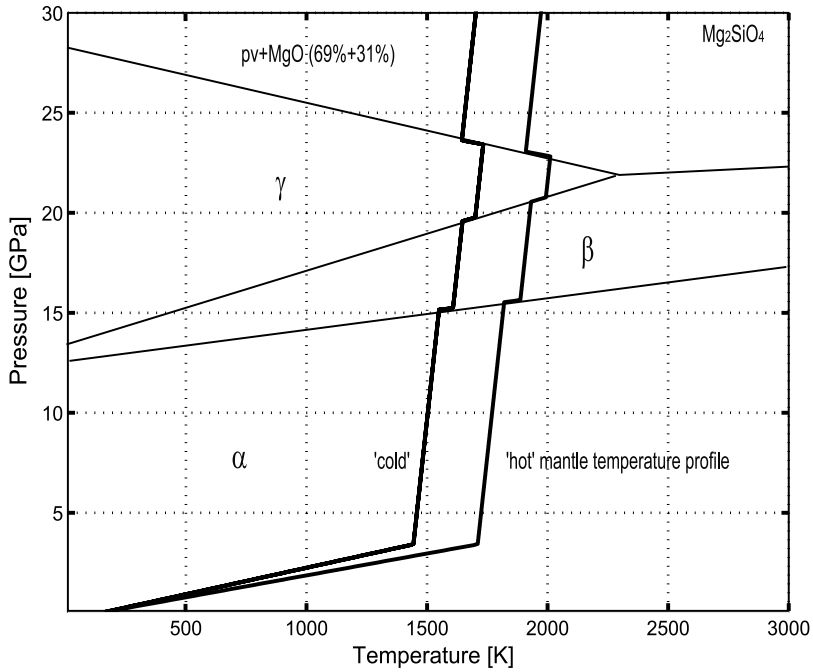


**Figure 2.** Phase diagram of $Mg_2SiO_4$ (thin lines) and mantle temperature profiles (thick lines) used as boundary conditions for the heat equation. Two mantle temperature models are tested. The "cold" model uses 1473 K as the temperature at the base of the lithosphere; the "hot" model uses 1723 K. The thickness of the lithosphere is 95 km. The adiabatic gradient is 0.3 K km$^{-1}$ in both models. The jumps in the temperature gradient are caused by latent heat released or consumed during phase transformations.

the momentum equation (1) can be solved independently. The independent solution to these equations requires less calculation time than a coupled solution.

[14] Temperature controls the locations of phase transformations in the slab and strongly influences the viscosity of the subducting lithosphere through the Arrhenius temperature dependence of rheological laws. The most important parameters determining temperature in the subducting slab are the temperature at the base of the oceanic lithosphere, the thermal gradient in the mantle, and the thickness of the lithosphere (determined mainly by its age at the onset of subduction).

[15] The thickness of the lithosphere and the temperature at the base of the lithosphere are estimated by inversions of seafloor depth and heat flow data versus age [*Stein and Stein*, 1992]. The temperature gradient in the mantle is assumed to be adiabatic, and the temperature at the boundary between the upper mantle and the lower mantle is constrained by laboratory measurements of the dissociation of spinel to perovskite and magnesiowüstite at the depth defined by seismological observations [*Ito and Takahashi*, 1989]. Because of uncertainties in these constraints, we tested two possible mantle temperature profiles. An adiabatic temperature gradient of 0.3 K $km^{-1}$ was used in both temperature models [*Turcotte and Schubert*, 1982], while the basal temperature was 1473 K for the "cold" model and 1723 K for the "hot" model [*Stein and Stein*, 1992] (Figure 2). We adopted the "plate" cooling model for the determination of the thickness of the lithosphere. In this model the thickness of the lithosphere is constant after a certain age. We use 95 km for the thickness and consider the lithosphere to be older than 70 Myr [*Stein and Stein*, 1992].

### 2.6. Pressure

[16] The preliminary reference Earth model [*Dziewonski and Anderson*, 1981] is used to convert pressure into depth.

### 2.7. Mineralogical Composition

[17] The main minerals that occur in the subducting lithosphere are olivine, pyroxene, and garnet and their high-pressure equivalents [*Ringwood*, 1982]. We assume a simplified mineralogical composition of the subducting slab and consider only the polymorphic transition of pure $Mg_2SiO_4$ $\alpha$ olivine to $\beta$ and $\gamma$ phases and the dissociation of $\gamma$ spinel to perovskite and magnesiowüstite (Figure 2). Different chemical compositions of olivine (the iron content) and phase transitions of other minerals are not considered in this work. The chemical composition of olivine containing iron mainly influences the depth of the phase transformation and also introduces two-phase fields [*Akaogi et al.*, 1989]. Phase transformations of pyroxene and garnet introduce more sources of volumetric strain at different depths in the subducting slab and influence the viscosity of the subducting slab [*Karato*, 1997].

[18] The stable phase boundaries are modeled using a linear *p-T* dependence:

$$p = P_0 + \frac{\Delta S}{\Delta V} T. \tag{9}$$

The parameter $P_0$, the change of entropy $\Delta S$, and the change of volume $\Delta V$ of appropriate phase reactions are assumed to be constant and are listed in Table 3.

**Table 3.** Thermodynamic Parameters

| Parameters | $\alpha$ to $\beta$ | $\beta$ to $\gamma$ | $\gamma$ to *pv + MgO* |
|---|---|---|---|
| Volume change of reaction ($\Delta V$), $cm^3$ $mol^{-1}$ | −3.16[a] | −0.98[a] | −2.59[b] |
| Entropy change of reaction ($\Delta S$), J $mol^{-1}$ $K^{-1}$ | −5.02[c] | −4.10[c] | 7.25[d] |
| Reference pressure ($P_0$) at $T = 0$ *K*, GPa | 12.057[c] | 12.640[c] | 28.360[d] |

[a]From *Akaogi et al.* [1989].
[b]From *Ito and Takahashi* [1989].
[c]Fit to Clapeyron curve in *p-T* space of *Akaogi et al.* [1989, Figure 3].
[d]Fit to Clapeyron curve in *p-T* space of *Ito and Takahashi* [1989, Figure 4].

[19] The latent heat $Q_L$ in equation (6) is determined by the pressure $p$ at which phase transformation occurs [*Devaux et al.*, 1997]:

$$Q_L = \frac{(p - P_0)}{V_m} \frac{\Delta V}{\Delta t}, \tag{10}$$

where $V_m$ is the molar volume of a mineral phase and $\Delta t$ is the time step of the calculation. Equations (9) and (10) must be solved together because they are coupled through the latent heat release that influences the temperature distribution in the slab and consequently the depth (i.e., pressure) of the phase transitions in the slab. The temperature and degree of phase transformation are then used as inputs to equations (1)–(5).

### 2.8. Elastic Constants

[20] The values of elastic parameters $K$ and $\mu$ at given *p-T* conditions are calculated from the following equations [*Goto et al.*, 1983]:

$$K(p,T) = K(0,0)\exp\left(-\gamma_r \int_0^T \alpha dT\right) + \left(\frac{\partial K(p,T)}{\partial p}\right)_T p \tag{11}$$

$$\mu(p,T) = \mu(0,0) + \left(\frac{\partial \mu(p,T)}{\partial p}\right)_T p + \left(\frac{\partial \mu(p,T)}{\partial T}\right)_p T, \tag{12}$$

where $\gamma_r$ is the Grüneisen parameter. Pressure and temperature derivatives of $\mu$ and $K$ are assumed to be constant, and values are given in Table 1.

### 2.9. Density

[21] The densities $\rho$ of minerals are estimated from the third order Birch-Murnaghan equation [*Goto et al.*, 1983; *Yoshioka et al.*, 1997; *Devaux et al.*, 2000].

### 2.10. Viscosity

[22] We consider only the dislocation creep and Peierls stress creep laws [e.g., *Kameyama et al.*, 1999]; these are dependent on temperature, pressure, and differential stress. An increase of temperature or stress tends to decrease viscosity, whereas an increase of pressure tends to increase viscosity. The rheology of rock also depends on grain size [*Karato et al.*, 2001] and volatile content. Grain size reduction in the subducting slab is expected to occur below the phase boundary where new grains grow [*Karato*, 1997]. Grain size reduction is dependent on grain growth rate and

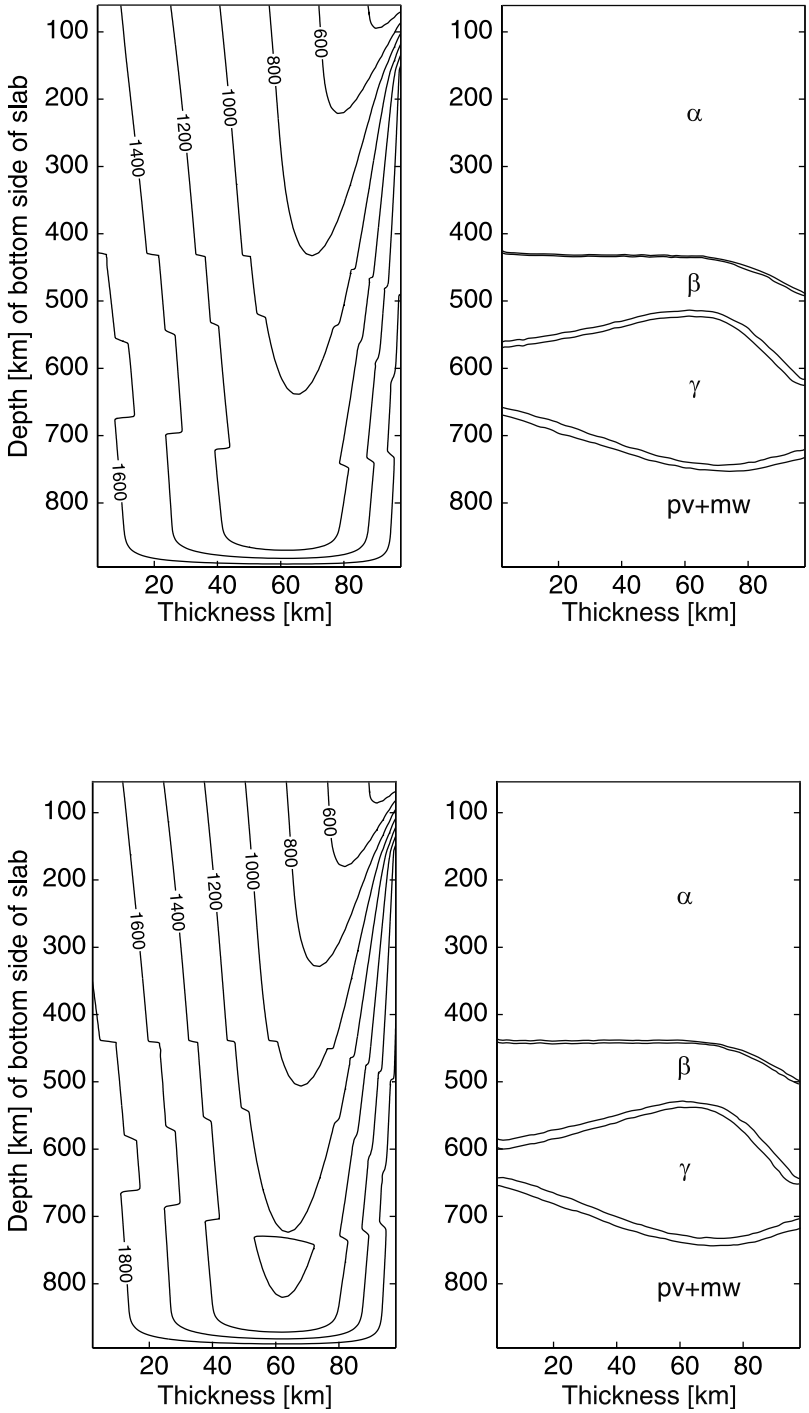


**Figure 3.** (left) Temperature (K) distribution and (right) phase boundaries in the subducting slab. Both (top) ''cold'' and (bottom) ''hot'' mantle temperature profiles were used to determine the temperature distribution inside the slab. Degrees of transformation 0.01 and 1 are shown for all phases. The numerals along the vertical axis denote depths of the bottom side of the slab. Notice that the same depth on the top side of the slab is shifted 61 km farther along the slab because of the dip of the slab. The horizontal and vertical axes are not to scale.

nucleation rate. Since the growth process is strongly dependent on temperature, the largest grain size reduction is expected in the coldest part of the slab. If the temperature is high enough, the phase transition occurs at depths that are close to equilibrium depths and grain size reduction is not significant [*Riedel and Karato*, 1997]. Since we assume equilibrium phase transitions in our model, we also assume that grain size reduction is not significant so that diffusion creep becomes negligible relative to dislocation creep. However, we test the influence of small grains on rheology

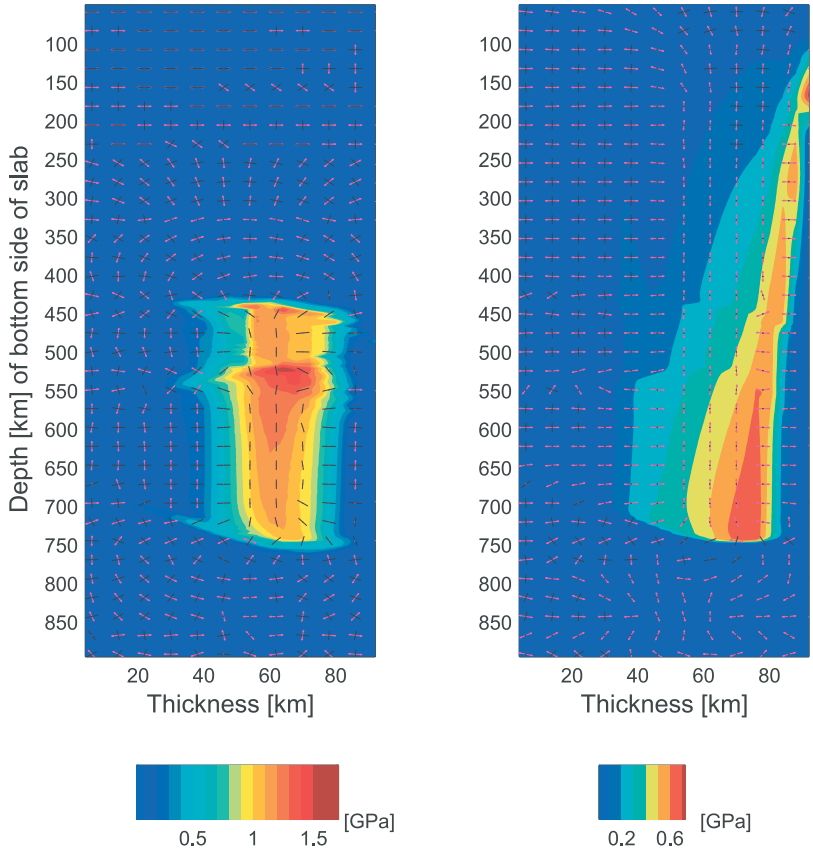


**Figure 4.** Distribution of shear stress and orientation of principal stress axes in the subducting slab. The (left) volumetric reduction term and the (right) thermal expansion term were used as sources of stress. The "cold" mantle temperature profile was used to determine the temperature inside the slab and the plane strain boundary condition was used to determine the stress distribution. The color scale represents the magnitude of shear stress. The orientation of the principal stress axis is shown by colored dashes: black and magenta dashes show the orientation of compression and extension, respectively. The orientation of the principal stress axis that is parallel to the trench is not plotted. The numerals along the vertical axis denote depths of the bottom side of the slab. The horizontal and vertical axes are not to scale.

by imposing a layer of low viscosity below the phase boundaries. The results will be discussed in section 3. The presence of volatiles in a subducting plate at transition zone depths is uncertain and we neglect it for simplicity.

[23] The relation for viscosity is

$$\nu = \frac{\sigma}{2\dot{\epsilon}}, \tag{13}$$

where $\sigma$ is the square root of the second invariant of the deviatoric stress and $\dot{\epsilon}$ is a strain rate determined either from a power law [*Frost and Ashby*, 1982; *Karato et al.*, 2001]

$$\dot{\epsilon} = C_1 \sigma^n \exp\left(\frac{-g_m T_m(p)}{T}\right), \quad \sigma \leq 200 \text{ MPa} \tag{14}$$

or from a Peierls stress law

$$\dot{\epsilon} = C_2 \exp\left[\frac{-g_m T_m(p)}{T}\left(1 - \frac{\sigma}{\sigma_P}\right)^2\right], \quad \sigma > 200 \text{ MPa} \tag{15}$$

where $T_m(p)$ is the pressure-dependent melting temperature of individual minerals [*Karato et al.*, 2001], $g_m$ is a constant proportional to activation energy, $\sigma_P$ is the Peierls stress, and $C_1$ and $C_2$ are preexponential coefficients for the power law and for Peierls stress law, respectively. Parameter values are given in Table 1. The Peierls stress creep law is not considered for perovskite because it is not well known. The Peierls stress creep law is also not considered for magnesiowüstite [*Frost and Ashby*, 1982] because it cannot be used without the Peierls stress creep law for perovskite.

[24] When two phases coexist, the parameters $K$, $\mu$, and $\dot{\epsilon}$ are weighted according to the degree of phase transformation. For the weighting of lower mantle minerals we use the fraction of molar volumes in the slab: 0.7 for perovskite and 0.3 for magnesiowüstite.

## 3. Results

### 3.1. Temperature and Phase Transformations

[25] Figure 3 shows the temperature distribution and degree of phase transformation in the slab for the two mantle temperature models. The mantle temperature models differ by 250 K, but this difference decreases inside the slab: the coldest temperature at, for example, 500 km depth is 900 K for the "cold" mantle temperature model and 1050 K

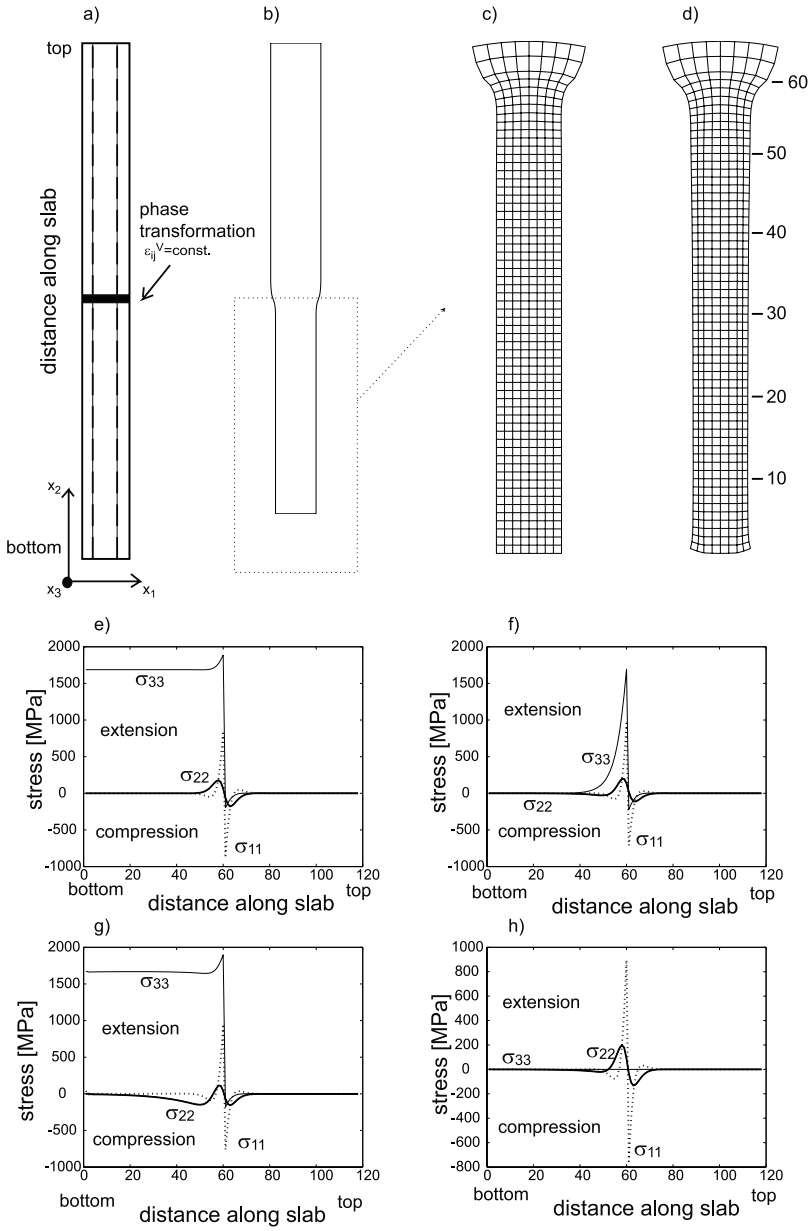


**Figure 5.** Results of test calculations to explain the slab shear stress distribution due to volumetric reductions. (a) Slab descends vertically into the mantle. The bold solid line shows the location of the only phase transformation. The dashed lines show the position of the relatively viscous core inside the slab that was used for Figures 5g and 5h. (b) Slab deformation according to the imposed volumetric reduction. The deformation shown is not to scale. The dotted rectangle shows the magnification of the grid deformation as shown in Figures 5c and 5d. (c) Deformed grid for the slab where a constant high viscosity was used ($\nu = 10^{29}$ Pa s). The grid below the phase transformation is deformed uniformly, and no shear stress occurs in the plane $x_1$, $x_2$. (d) Deformed grid for the slab where a constant high viscosity was used in the center of the slab ($\nu = 10^{27}$ Pa s) and a low viscosity was used at the boundaries ($\nu = 10^{24}$ Pa s). The grid below the phase transformation is deformed nonuniformly so the shear stress occurs in the plane $x_1$, $x_2$. The numerals indicate the distance along the slab given by the grid point number. (e) Magnitude of $\sigma_{11}$ (dotted line), $\sigma_{22}$ (bold solid line), and $\sigma_{33}$ (solid line) along the center of the slab (parallel to $x_2$ axis). Viscosity is constant everywhere ($\nu = 10^{29}$ Pa s). (f) Similar to Figure 5e, but viscosity is constant everywhere at $\nu = 10^{24}$ Pa s. (g) Similar to Figure 5e, but a high viscosity was used in the center of the slab ($\nu = 10^{27}$ Pa s) and a low viscosity was used at the boundaries ($\nu = 10^{24}$ Pa s). (h) Same as Figure 5g, but for the plane stress boundary condition.

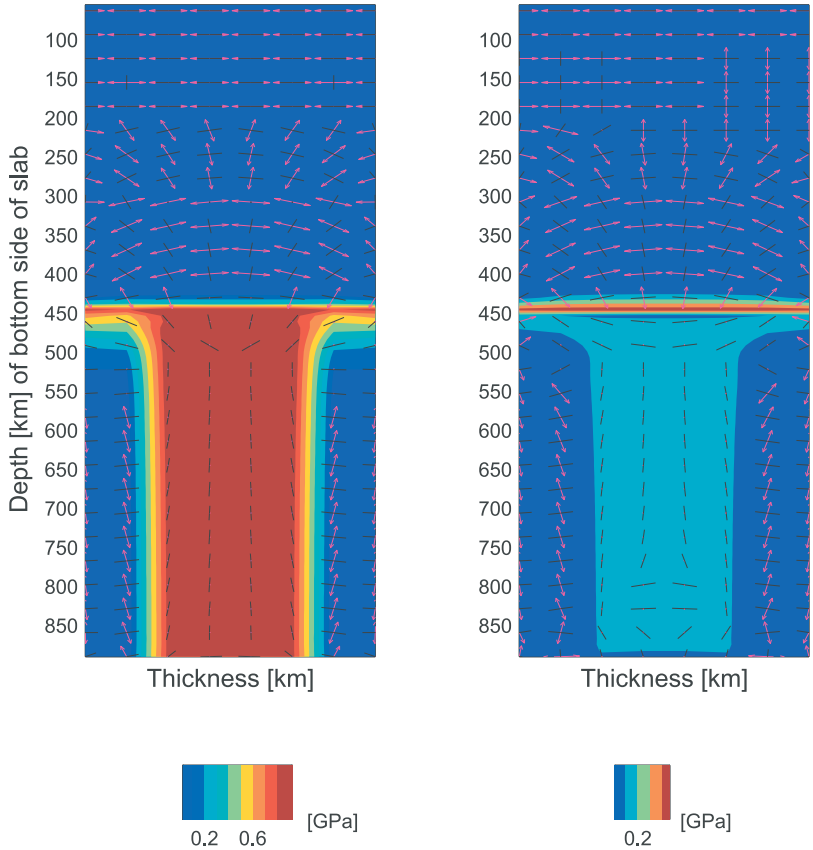


**Figure 6.** Test of the effect of a low-viscosity horizontal layer on stress. The figure shows the distribution of shear stress and the orientation of principal stress axes in the vertically descending slab. The only phase transformation occurs at 450 km depth. (left) High viscosity in the center of the slab ($\nu = 10^{27}$ Pa s) and low viscosity at the boundaries ($\nu = 10^{24}$ Pa s). (right) Same viscosity distribution, but with a low-viscosity layer ($\nu = 10^{23}$ Pa s) at 440–460 km depth. The layer simulates the relaxation by diffusion creep caused by the presence of small grains below the phase boundary. The color scale represents the magnitude of shear stress. The orientation of the principal stress axis is shown by colored dashes: black and magenta dashes show the orientation of compression and extension, respectively. The orientation of the principal stress axis that is parallel to the trench is not plotted. The numerals along the vertical axis denote depths of the bottom side of the slab. The horizontal and vertical axes are not to scale.

for the "hot" mantle temperature model. Even though we tested two different mantle temperature models, we obtain very similar mineralogical fields inside the slab that differ mainly in the extent of the stability fields of β and γ spinel. This is due to the fact that different mantle temperature profiles intersect the phase boundaries at different pressures (see Figure 2). The mantle temperature profiles are thus not very important for the location of phase boundaries, but they can be crucial for determination of viscosity.

### 3.2. Stress

[26] We calculate the stress distribution in the subducting slab for the following cases: (1) two source terms, the thermal expansion term and the volumetric reduction term, given by equations (4) and (5), respectively; (2) two different mantle temperature profiles, "cold" and "hot"; and (3) two different boundary conditions in the $x_3$ direction, plane strain and plane stress.

[27] The stress distributions in the slab due to the volumetric reduction term and the thermal expansion term are shown in Figure 4. The "cold" mantle temperature profile and the plane strain boundary condition were used. The shear stress due to volumetric reduction is approximately twice the stress caused by thermal expansion. While the shear stress due to the volumetric reductions is restricted to the depth range 400–700 km, the shear stress due to thermal expansion occurs from the top of the slab to 700 km depth. The orientation of principal stress axes due to volumetric reduction is characterized by compression oriented along the dip of the slab and tension parallel to the trench. The orientation of tension along a trench is determined by the two-dimensional structure of a slab. In contrast, the orientation of principal stress axes due to thermal expansion is characterized by tension oriented along the dip of the slab and compression parallel to the trench.

[28] We ran tests with simplified conditions in the subducting slab in order to explain the observed stress distribution: Is the observed shear stress caused by a nonuniform distribution of sources of stress (e.g., the term given by equation (4)) or by nonuniform relaxation of stress? Why does volumetric reduction yield compression oriented along the dip of the slab?

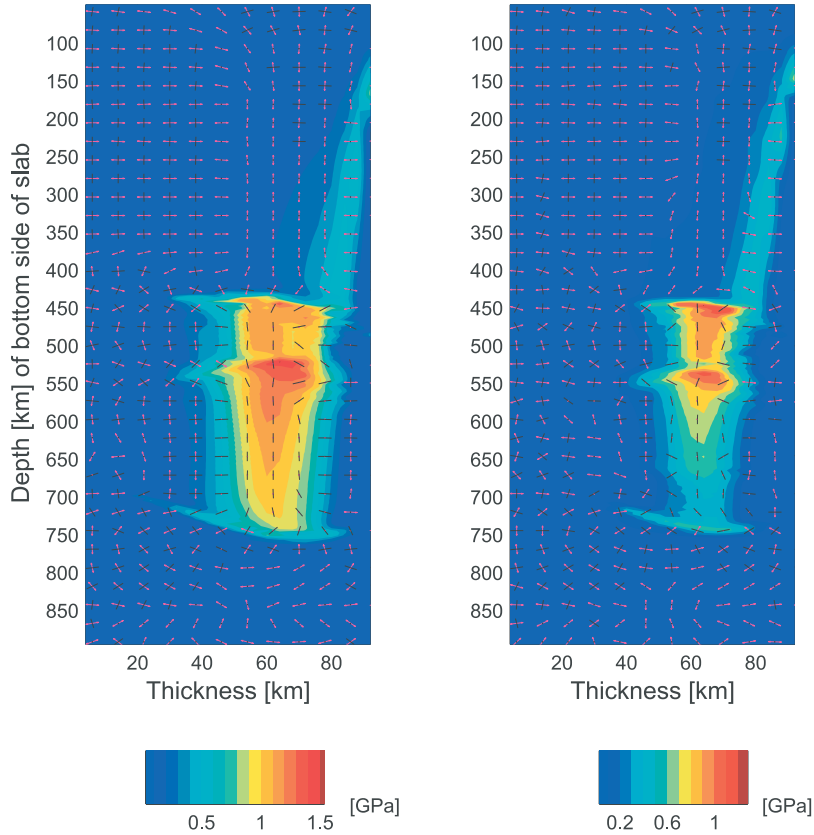


**Figure 7.** Distribution of shear stress and orientation of principal stress axes in the subducting slab. (left) "Cold" mantle temperature profile used to determine the temperature inside the slab and the plane strain boundary condition used to determine the stress distribution. (right) "Hot" mantle temperature profile used to determine the temperature inside the slab and the plane strain boundary condition used to determine the stress distribution. Both the volumetric reduction term and the thermal expansion term were used as sources of stress. The color scale represents the magnitude of the shear stress. The orientation of the principal stress axis is shown by colored dashes: black and magenta dashes show the orientation of compression and extension, respectively. The orientation of the principal stress axis that is parallel to the trench is not plotted. The numerals along the vertical axis denote depths of the bottom side of the slab. The horizontal and vertical axes are not to scale.

[29] First, we tested the effect of the nonuniform distribution of sources of stress. The viscosity was held constant everywhere and only the magnitude of the source term $\epsilon_{ij}^{V}$ varied according to the temperature and pressure in the subducting lithosphere (see section 2.9). No shear stress is produced by a nonuniform distribution of source of stress, so the stress caused by volumetric reductions must be caused by a nonuniform relaxation of stress, that is, by viscosity variations. We also tested the flat or curved shapes of phase boundaries; no shear stresses are produced in this case either.

[30] Second, we tested a slab dipping 90° into the mantle with only one phase boundary at a certain constant depth (Figure 5a). During the phase transformation the volumetric reduction was held constant, that is, $\epsilon_{ij}^{V}$ was constant, the thermal expansion was $\epsilon_{ij}^{T} = 0$, and the elastic constants $K$ and $\mu$ were held constant. We studied the stress distribution in the slab for the following viscosity distributions: (1) when viscosity in the slab was high everywhere ($\nu = 10^{29}$ Pa s); (2) when viscosity in the slab was low everywhere ($\nu = 10^{24}$ Pa s); and (3) a high viscosity ($\nu = 10^{27}$ Pa s) in a strip inside the slab and a low viscosity ($\nu = 10^{24}$ Pa s) on the boundaries of the slab (Figure 5a). We assumed the plane strain boundary condition. In all three cases the stress is 0 at depths shallower than the phase boundary (distance along slab >70, see Figure 5). Near the phase boundary, stresses are nonzero (distance along slab from 50 to 70) and are related to the narrowing of the slab in this region. Interestingly, stresses stay nonzero below this region (<50) in some of the studied cases. In case 1 the stress components $\sigma_{11}$ and $\sigma_{22}$ are zero. The stress component $\sigma_{33}$ is tensional and its magnitude is high because the boundary condition in the $x_3$ direction does not allow any displacement in this direction, while at the same time the internal strain forces the slab to shrink (Figures 5b, 5c, and 5e). In case 2 all stress components are relaxed except in the narrow region just below the phase boundary (Figure 5f). In case 3, $\sigma_{33}$ is tensional, $\sigma_{11}$ is zero, and $\sigma_{22}$ is compressional in the center of the slab, whereas there is no stress on the boundaries of the slab where the viscosity is small. The displacement on the boundaries of the slab is larger than in the center, which causes the downdip compression (in the $x_2$ direction) in the center of the slab (Figures 5d and 5g).

[31] The magnitude of the downdip compression depends on the viscosity contrast across the slab and on the thickness

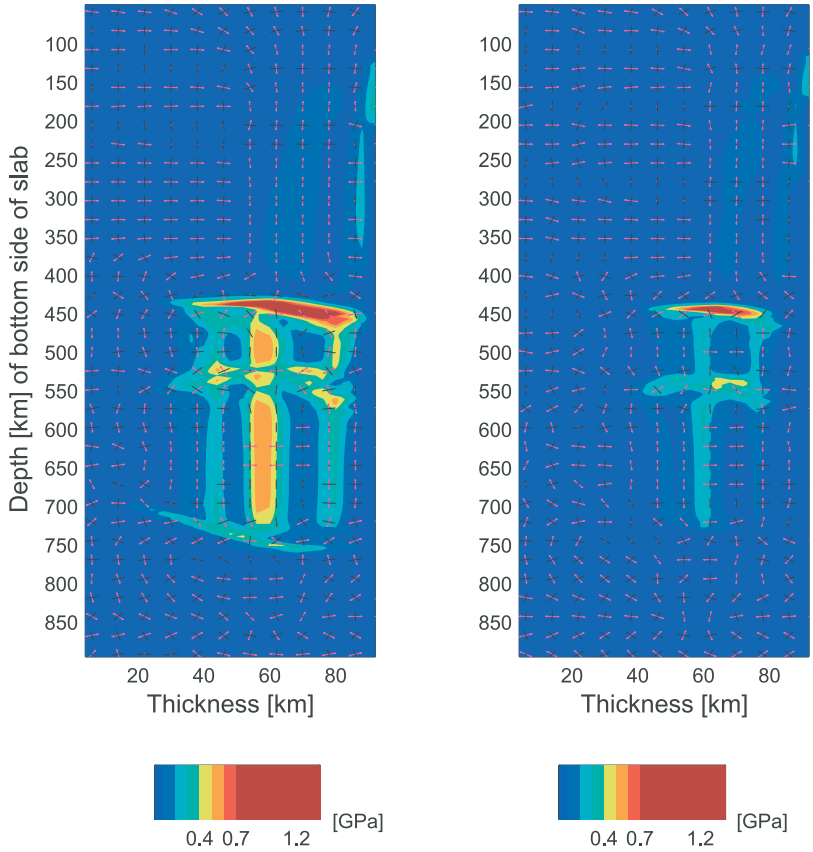


**Figure 8.** Same as Figure 7, but for the plane stress boundary condition.

of the central strip. If the boundaries (region outside the strip) are too weak (i.e., with a low viscosity of $\sim 10^{22}$ Pa s) or too narrow ($\sim$10 km) for the same magnitude of the source of stress, they do not produce any stress in the center of the slab. We repeated the calculations in case 3 but with the plane stress boundary condition. The stress components $\sigma_{33}$ and $\sigma_{11}$ are zero and $\sigma_{22}$ is compressional (Figure 5h). The compression, though much smaller than in the same case with the plane strain boundary condition, nevertheless persists.

[32] Third, we tested the influence of a low-viscosity horizontal layer on the stress distribution, simulating the effect of grain size reduction after phase transformation. The model we used was the same as used in case 3 above, but a 20-km-thick low-viscosity layer ($\nu = 10^{23}$ Pa s) was imposed below the phase boundary. The result is shown in Figure 6. The shear stress relaxes where the low-viscosity layer occurs. Depending on the thickness of the layer and on its viscosity, the stress is relaxed partly or completely. When the stress is not completely relaxed, the orientation of the principal stress axes remains the same as in the case without a low-viscosity layer.

[33] The test runs explain the occurrence of downdip-oriented compression in the slab. As the slab descends into the transition zone, the volumetric reduction due to the $\alpha$ olivine to $\beta$ spinel phase transformation causes deformation of the lithosphere. Since the final deformation is nonuniform due to the nonuniform viscosity of the slab, shear stress occurs. This shear stress is relaxed during descent into the deeper mantle until the next phase transformation is encountered. In our model the next phase transformation is $\beta$ to $\gamma$ spinel, occurring at a depth of $\sim$500–550 km. There, the shear stress due to $\beta \rightarrow \gamma$ is added to the unrelaxed stress from the previous phase transformation. The shear stress survives to a depth determined by creep relaxation parameters: the depth is not only determined by the viscosity contrast inside the slab, as discussed in section 3.2, but also by the pressure dependence of viscosity (through the pressure dependence of the activation energy in creep laws). In our model, shear stress survives to the depth of the upper mantle-lower mantle transition. No shear stress is caused by the volumetric strain due to dissociation of $\gamma$ spinel to perovskite and magnesiowüstite because in our model there is no viscosity contrast within the slab when it is in the lower mantle and also because the slab viscosity there is low, so it relaxes stresses.

[34] The stress distribution in the slab when both source terms, a "cold" mantle temperature profile, and a plane strain boundary condition were considered is shown in Figure 7 (left). Shear stresses as large as 1.5 GPa occur in the depth range 400–700 km in the central part of the slab where the viscosity is large. The depths are different from the depths of phase transformations in the mantle because of the elevation and depression of phase boundaries inside the slab. The shear stress is caused by the volumetric reduction of the phase transformation of $\alpha$ olivine to $\beta$ and $\gamma$ spinel. The orientation of principal stress axes is characterized by a compression oriented along the dip of the slab and a tension parallel to the trench. The stress distribution for the same model but for a "hot" mantle temperature is also shown in Figure 7 (right). The stress field is very similar; the stresses

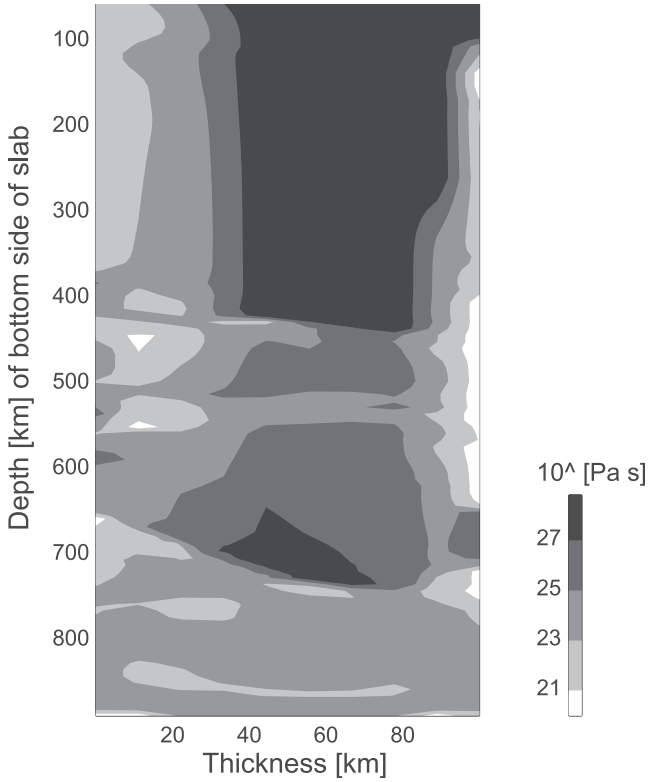


**Figure 9.** Viscosity distribution in the subducting slab. The "cold" mantle temperature profile was used to determine the temperature inside the slab, and the plane strain boundary condition was used to determine the stress distribution. Both the volumetric reduction term and the thermal expansion term were used as sources of stress. The numerals along the vertical axis denote depths of the bottom side of the slab. The horizontal and vertical axes are not to scale.

relax twice as fast as in the case of the cold mantle profile (Figure 7, left).

[35] The stress field for a "cold" mantle temperature profile and plane stress boundary condition is shown in Figure 8 (left). The shear stress occurs in the depth range 400–700 km with a maximum of ~1.4 GPa at 440 km depth. Below this depth, shear stress relaxes rapidly with increasing depth, and the highest shear stress of only 0.6 GPa occurs in the narrow cold center of the slab. The principal stress axes are characterized by a compression oriented along the dip of the slab and a tension in the plane perpendicular to compression. The shear stress for the same model but for a "hot" mantle temperature is shown in Figure 8 (right). The stress field is again similar, but the magnitude of the shear stress is lower.

[36] We also tested the influence of the γ spinel to perovskite and magnesiowüstite transformation on stresses in the slab. Since the stress from the γ spinel to perovskite and magnesiowüstite would arise below the phase boundary, the stress field in the transition zone is not significantly influenced by this phase transformation. This is discussed in more detail in section 5.

[37] In all the models described so far the shear stress occurs in the depth range 400–700 km. The compression axis is oriented down-dip, whereas the extension axis is either trench-parallel or in the plane perpendicular to the compression axis. The magnitude of the shear stress varies according to the mantle temperature and stress boundary condition.

### 3.3. Viscosity

[38] The viscosity distribution in the subducting plate is shown in Figure 9 for the model with a plane strain boundary condition and a "cold" mantle temperature profile. Viscosity is highest in the central part of the subducting slab because the temperature is low there. Viscosity increases with depth due to the pressure dependence of the rheological law, but it decreases in the parts of the slab where the stresses due to phase transformations are concentrated. The viscosity in our model slab ranges from $10^{20}$ to $10^{29}$ Pa s (the upper limit can be considered as elastic behavior). The stress persists in places where viscosity is higher than $\sim 10^{24}$ Pa s. The viscosity is generally 2 orders of magnitude lower in the model where the "hot" mantle temperature profile was considered.

[39] The range of viscosity in our model is very similar to the range of viscosity used in *Karato et al.*'s [2001] model. The distribution of viscosity is similar too, although some differences arise below the phase transitions due to the different phase transitions and strains considered.

## 4. Comparison With Seismic Observations in Tonga

[40] We compared the state of stress in our model with seismic observations of the Tonga Wadati-Benioff zone in the region 179°–185°E and 22°–20°S. The dip, velocity of subduction, and age of subduction in Tonga agree with the input parameters in our model. We use the Harvard centroid moment tensor solutions for orientations of *P*, *B*, and *T* axes as well as for the locations of hypocenters. The *P*, *B*, and *T* axes are shown in a cross section in Figure 10. We compare

**Figure 10.** (opposite) Comparison of our model with seismic observations. (top) Shear stress and orientation of principal stress axes in the subducting slab. The "cold" mantle temperature profile was used to determine the temperature inside the slab and the plane strain boundary condition was used to determine the stress distribution. Both the volumetric reduction term and the thermal expansion term were used as sources of stress. The color scale represents the magnitude of shear stress. The orientation of the principal stress axis is shown by colored dashes: black and magenta dashes show the orientation of compression and extension, respectively. The orientation of the principal stress axis that is parallel to the trench is not plotted. The horizontal and vertical axes are to scale. (bottom) Orientation of *P* (black dashes), *B* (green dashes), and *T* (red dashes) axes in the Tonga subducting slab projected on the plane of the cross section. Length of a bar is determined by the cosines of the angle between the azimuth of the cross section and the azimuth of the axis. The azimuth of the cross section is 250°. Data are taken from the Harvard centroid moment tensor solutions.

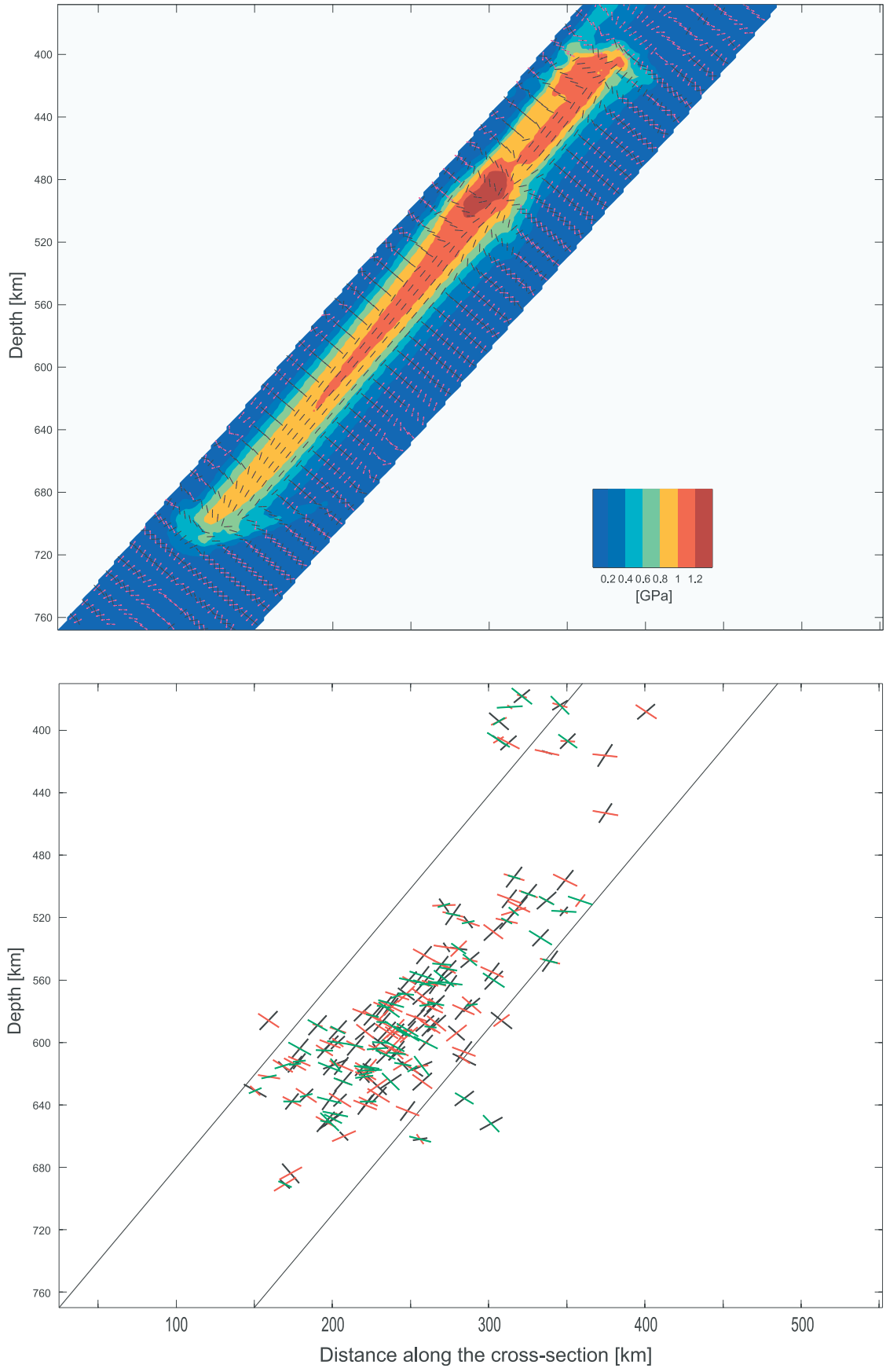
Depth [km]
400
440
480
520
560
600
640
680
720
760
0.2 0.4 0.6 0.8 1 1.2
[GPa]
Depth [km]
400
440
480
520
560
600
640
680
720
760
100
200
300
400
500
Distance along the cross-section [km]

our model only with data below 300 km, where the model is not influenced by the boundary condition at the trench.

[41] Seismic activity in the studied region (deeper than 300 km) is lowest in the depth ranges ~300–370 km and ~440–480 km and is highest in the depth ranges ~370–440 km and ~480–670 km. Our model predicts high shear stress in the depth range 400–700 km with two maxima, one below the uppermost phase transformation of $\alpha$ olivine to $\beta$ spinel at 400 km depth and the other one below the phase transformation of $\beta$ spinel to $\gamma$ spinel at 480 km depth. The depth range of the modeled shear stress fits the observations well, except for the depth of the upper maximum of shear stress. This depth is influenced by our simplified chemical composition of olivine. The iron in olivine moves the phase boundary ~20 km shallower [*Akaogi et al.*, 1989; *Bina*, 1997]. Also, the increase in seismic activity in the depth range 560–640 km is not predicted by our model.

[42] In our model, compression is oriented down-dip in the depth range where the shear stress is the highest. This agrees well with the orientation of *P* axes in the Tonga Wadati-Benioff zone [*Jiao et al.*, 2000] and also with observations of *P* axes worldwide in this depth range [*Isacks and Molnar*, 1971]. The extension is parallel to the trench or perpendicular to the compression axis in our model, depending on the boundary condition used in the direction parallel to trench. This agrees with observations of *B* and *T* axes in Tonga, both of which are parallel to the trench [*Jiao et al.*, 2000]. However, the *B* axis parallel to the trench is more common in worldwide observations [*Isacks and Molnar*, 1971].

[43] In our model the orientation of the principal stress axes does not vary significantly. The most remarkable variations can be found below phase boundary at 400 km and 480 km. This might correspond to the variations of *P* axes in Tonga at depths 400 km and 520 km (Figure 10). However, the variations at 400 km depth are more probably explained by a double seismic layer [*Wiens et al.*, 1993]. Generally, the variations of the state of stress below phase boundaries when compared with variations of the *P*, *B*, and *T* axes in the subducting lithosphere could be a useful tool for understanding phase changes in the subducting lithosphere and will be the subject of further investigation.

## 5. Discussion

[44] High shear stress in the depth range 400–700 km is well correlated with the occurrence of deep earthquakes [e.g., *Isacks and Molnar*, 1971; *Green and Houston*, 1995]. High shear stress is undoubtedly a trigger of earthquakes, even though the mechanism of releasing stress to produce an earthquake at this depth is unknown. Since our model produces high shear stress in the transition zone for equilibrium phase transformations, it is not necessary to explain high shear stress by metastability of olivine [*Green and Houston*, 1995]. However, the release of stress by deep earthquakes may require transformational faulting associated with a metastable olivine wedge. Other mechanisms such as dehydration embrittlement, shear instability, ductile faulting, or crystallographic shear not associated with metastability of olivine may be responsible for deep earthquakes [see, e.g., *Kirby et al.*, 1996].

[45] The maximum stress drop observed in the Bolivian earthquake in 1994 was 0.11 GPa [*Kanamori et al.*, 1998]. The magnitude of the maximum model shear stress (1.4 GPa) that occurs just below the phase boundary at 480 km depth is much larger than the stress drops observed in individual earthquakes. The shear stress magnitudes in the rest of the transition zone vary according to the model: 0.9–1.2 GPa for plane strain and a "cold" mantle temperature profile and 0.5–0.7 GPa for a "hot" mantle temperature profile; 0.5 GPa for plane stress and a "cold" mantle temperature profile and 0.3 GPa for a "hot" mantle temperature profile. The latter values are more in accord with observed earthquake stress drops.

[46] The magnitude of the model shear stress depends on the volumetric strains $\epsilon_{ij}^{V}$. The volumetric strains do not involve a large uncertainty because they are calculated from mineral densities, and thus the only way to decrease the shear stress is through the rheological law. Obviously, the magnitude of shear stress can be significantly decreased by using hotter mantle temperature profiles. Another possibility is to decrease the Peierls stress for transition zone minerals because when the shear stress is high, the Peierls stress creep mechanism controls deformation. The Peierls stress of olivine is 8.5 GPa; the Peierls stress of spinel is not known precisely, but it is assumed to be 10 GPa [*Karato et al.*, 2001]. We decreased the value of the Peierls stress of spinel to 9 GPa, but the magnitude of shear stress did not decrease significantly. Without using a Peierls stress law (i.e., using only dislocation creep), the magnitude of maximum shear stress is >3 GPa. Reduction of grain size after phase transformation would decrease the shear stress significantly. *Kanamori et al.* [1998] showed that the efficiency of deep earthquakes is low, implying that the magnitude of stress drops in the slab must be significantly smaller than the magnitude of stress in the slab.

[47] A coupled solution of the momentum equation (1) and the heat equation (6) could change the stress results. The shear heating term, which could be included in the heat equation, would affect temperature; in turn, temperature would affect viscosity and therefore the strain rate. The strain rate would then influence shear heating. The effect of the thermal-mechanical coupling is difficult to assess due to the nonlinearity of the term, but we might expect that shear heating would be localized below phase boundaries. However, the additional heat produced by this term can be compared with the latent heat released at the phase boundaries. From our analysis we know that latent heat does not influence the viscosity because the Peierls stress creep law, which is mainly sensitive to the shear stress, is the weakest creep mechanism acting below the phase boundaries. Thus the shear heating term might not play a crucial role in the subducting slab.

[48] The resulting stresses associated with the phase changes in the slab influence the pressure in the slab and thus the location of the phase transformations. The pressure drop related to the volumetric reductions for the "cold" model is ~1.2 GPa, which corresponds to a change in depth of 36 km. The pressure drop for the "hot" model is ~400 MPa, which corresponds to a depth change of 12 km. This is a maximum estimate since some of the stress could be relaxed by plastic creep during the phase transformation. The estimate for the "hot" model is low because part of the

pressure drop is relaxed due to the low viscosity in this model.

[49] The magnitude of the phase change-induced shear stresses could be decreased by adopting a temperature-dependent thermal conductivity. Temperature dependence of the thermal conductivity would increase the temperature inside the slab by ~100 K [*Hauck et al.*, 1999]. This would decrease the viscosity in the slab and therefore the shear stress, as well.

[50] Our model provides an explanation for stresses that can cause deep earthquakes. Validity of our stress model is dependent on a better knowledge of parameters determining the viscosity inside the subducting lithosphere, that is, temperature and grain size. Our model explains earthquakes with *P* axes slab dip-parallel and *T* axes parallel to the trench. These events may be caused by volumetric reductions due to phase transformations. The events with *P* axes oriented along the dip of the plate and *T* axes perpendicular to the slab plane are not predicted by the plane strain model, but they can occur in the model with the plane stress boundary condition.

[51] Our model does not show any shear stress at lower mantle depths. This is caused by the fact that our model viscosity at these depths does not allow shear stress to persist there. Thus our stress field provides no information about the penetration of the subducting slab into the lower mantle. If our stresses are reflected in the seismic activity observed in the Wadati-Benioff zones, then *P*, *B*, and *T* axes cannot be used for the interpretation of slab dynamics. Our model is limited to subducting plates that descend straight through the upper mantle and into the lower mantle. Subducting plates that are strongly deformed upon interaction with the lower mantle, as shown by seismic tomography, must be affected by other sources of stress such as buoyancy and viscous resistance on the sides and leading edge of the plate. Since our stress model is simplified and dependent on knowledge of parameters determining the viscosity inside the subducting lithosphere, as mentioned above, it is possible that shear stresses due to equilibrium phase changes in the transition zone will relax at shallower depths than they do in our model, and other sources of stress, for example, buoyancy forces, will become more important at these depths.

## 6. Conclusions

[52] 1. Volumetric reductions due to equilibrium phase transformations cause high shear stress in the transition zone because of the variable viscosity inside the subducting slab. Model shear stresses arising from these volumetric reductions are in agreement with observations of high seismic activity in the Tonga Wadati-Benioff zone. Compression is oriented along the dip of the slab, and extension is oriented in the plane perpendicular to the compression axis.

[53] 2. Since our model stresses are in qualitative agreement with the seismic observations, and because the model stresses are higher than those caused by buoyancy forces, our model provides a possible explanation of the stresses causing deep earthquakes. Also, our model does not need metastability of olivine to explain the occurrence of high shear stress in the transition zone. The model thus provides a simple explanation for the stress causing deep earthquakes. However, the model says nothing about the actual mechanisms by which failure occurs in deep earthquakes.

[54] **Acknowledgments.** We thank W. Moore, H. Houston, and S.-I. Karato for helpful discussions. Reviews from D. Yuen and S.-I. Karato helped to improve the manuscript considerably. This research was supported by a grant from the Los Alamos branch of the Institute of Geophysics and Planetary Physics.

## References

Akaogi, M., A. Navrotsky, T. Yagi, and S. Akimoto, Pyroxene-garnet transformation: Thermochemistry and elasticity of garnet solid solutions, and application to a pyrolite mantle, in *High-Pressure Research in Mineral Physics*, *Geophys. Monogr. Ser.*, vol. 39, edited by M. H. Manghnani and Y. Syono, pp. 251–260, AGU, Washington, D. C., 1987.

Akaogi, M., E. Ito, and A. Navrotsky, The olivine-modified spinel-spinel transitions in the system $Mg_2SiO_4$-$Fe_2SiO_4$ calorimetric measurements, thermomechanical calculation and geophysical application, *J. Geophys. Res.*, *94*, 15,671–15,685, 1989.

Anderson, O. L., and D. G. Isaak, Elastic constants of mantle minerals at high temperature, in *A Handbook of Physical Constants: Mineral Physics and Crystallography*, *AGU Ref. Shelf Ser.*, vol. 2, edited by I. J. Ahrens, pp. 64–97, AGU, Washington, D. C., 1995.

Bina, C. R., Phase transition buoyancy contributions to stresses in subducting lithosphere, *Geophys. Res. Lett.*, *23*, 3563–3566, 1996.

Bina, C. R., Patterns of deep seismicity reflect buoyancy stresses due to phase transitions, *Geophys. Res. Lett.*, *24*, 3301–3304, 1997.

Cherukuri, H. P., and T. G. Shawki, An energy-based localization theory: II. Effects of the diffusion inertia, and dissipation numbers, *Int. J. Plast.*, *11*, 41–64, 1995.

Devaux, J. P., G. Schubert, and C. Anderson, Formation of a metastable olivine wedge in a descending slab, *J. Geophys. Res.*, *102*, 24,627–24,637, 1997.

Devaux, J. P., L. Fleitout, G. Schubert, and C. Anderson, Stresses in a subducting slab in the presence of a metastable olivine wedge, *J. Geophys. Res.*, *105*, 13,365–13,373, 2000.

Duffy, T. S., and D. L. Anderson, Seismic velocities in mantle minerals and the mineralogy of the upper mantle, *J. Geophys. Res.*, *94*, 1895–1912, 1989.

Dziewonski, A. M., and D. L. Anderson, Preliminary reference Earth model (PREM), *Phys. Earth Planet. Inter.*, *25*, 297–356, 1981.

Frost, H. J., and M. F. Ashby, *Deformation-Mechanism Maps*, 168 pp., Pergamon, New York, 1982.

Goetze, C., and B. Evans, Stress and temperature in the bending lithosphere as constrained by experimental rock mechanics, *Geophys. J. R. Astron. Soc.*, *59*, 463–478, 1979.

Goto, K., H. Hamaguchi, and Z. Suzuki, Distribution of stress in descending plate in special reference to intermediate and deep focus earthquakes, I. Characteristics of thermal stress distribution, *Tohoku Geophys. J.*, *29*, 81–105, 1983.

Goto, K., Z. Suzuki, and H. Hamaguchi, Earthquake generating stresses in a descending slab, *Tectonophysics*, *112*, 111–128, 1985.

Goto, K., Z. Suzuki, and H. Hamaguchi, Stress distribution due to olivine-spinel phase transition in descending plate and deep focus earthquakes, *J. Geophys. Res.*, *92*, 13,811–13,820, 1987.

Green, H. W., and H. Houston, The mechanics of deep earthquakes, *Ann. Rev. Earth Planet. Sci.*, *23*, 169–213, 1995.

Hauck, S. A., II, R. J. Phillips, and A. M. Hofmeister, Variable conductivity: Effects on the thermal structure of subducting slabs, *Geophys. Res. Lett.*, *26*, 3257–3260, 1999.

Isaak, D. G., O. L. Anderson, T. Goto, and I. Suzuki, Elasticity of single-crystal forsterite measured to 1700 K, *J. Geophys. Res.*, *94*, 5895–5906, 1989.

Isacks, B., and P. Molnar, Distribution of stresses in the descending lithosphere from a global survey of focal-mechanism solutions of mantle earthquakes, *Rev. Geophys.*, *9*, 103–174, 1971.

Ito, E., and E. Takahashi, Postspinel transformations in the system $Mg_2SiO_4$-$Fe_2SiO_4$ and some geophysical implications, *J. Geophys. Res.*, *94*, 10,637–10,646, 1989.

Jeanloz, R., and A. B. Thompson, Phase transitions and mantle discontinuities, *Rev. Geophys.*, *21*, 51–74, 1983.

Jiao, W., P. G. Silver, Y. Fei, and C. T. Prewitt, Do intermediate- and deep-focus earthquakes occur on preexisting weak zones? An examination of the Tonga subduction zone, *J. Geophys. Res.*, *105*, 28,125–28,138, 2000.

Kameyama, M., D. A. Yuen, and S.-I. Karato, Thermal-mechanical effects of low-temperature plasticity (the Peierls mechanism) on the deformation of a viscoelastic shear zone, *Earth Planet. Sci. Lett.*, *168*, 159–172, 1999.

Kanamori, H., D. L. Anderson, and T. H. Heaton, Frictional melting during the rupture of the 1994 Bolivian earthquake, *Science*, *279*, 839–842, 1998.

Karato, S., Phase transformations and rheological properties of mantle minerals, in *Earth's Deep Interior: The Doornbos Memorial Volume*, edited by D. J. Crossley, pp. 223–272, Gordon and Breach, Newark, N. J., 1997.

Karato, S., M. R. Riedel, and D. A. Yuen, Rheological structure and deformation of subducted slabs in the mantle transition zone: Implications for mantle circulation and deep earthquakes, *Phys. Earth Planet. Inter.*, *127*, 83–108, 2001.

Kirby, S. H., S. Stein, E. Okal, and D. C. Rubie, Metastable mantle phase transformations and deep earthquakes in subducting oceanic lithosphere, *Rev. Geophys.*, *34*, 261–306, 1996.

Larsen, T. B., and D. A. Yuen, Fast plumeheads: Temperature-dependent versus non-Newtonian rheology, *Geophys. Res. Lett.*, *24*, 1995–1998, 1997.

Madariaga, R., Dynamics of an expanding circular fault, *Bull. Seismol. Soc. Am.*, *66*, 163–182, 1976.

Presnall, D. C., and M. J. Walter, Melting of forsterite, $Mg_2SiO_4$, from 9.7 to 16.5 GPa, *J. Geophys. Res.*, *98*, 19,777–19,783, 1993.

Regenauer-Lieb, K., and D. A. Yuen, Quasi-adiabatic instabilities associated with necking processes of an elasto-viscoplastic lithosphere, *Phys. Earth Planet. Inter.*, *118*, 89–102, 2000.

Riedel, M. R., and S. Karato, Grain-size evolution in subducted oceanic lithosphere associated with the olivine-spinel transformation and its effects on rheology, *Earth Planet. Sci. Lett.*, *148*, 27–43, 1997.

Ringwood, A. E., Phase transformations and differentiation in subducted lithosphere: Implications for mantle dynamics, basalt petrogenesis, and crustal evolution, *J. Geol.*, *90*, 611–643, 1982.

Sawamoto, H., D. J. Weidner, S. Sasaki, and M. Kumazawa, Single-crystal elastic properties of the modified spinel (beta) phase of magnesium orthosilicate, *Science*, *224*, 749–751, 1984.

Schubert, G., C. Froidevaux, and D. A. Yuen, Oceanic lithosphere and asthenosphere: Thermal and mechanical structure, *J. Geophys. Res.*, *81*, 3525–3540, 1976.

Stein, C. A., and S. Stein, A model for the global variation in oceanic depth and heat flow with lithospheric age, *Nature*, *359*, 123–129, 1992.

Stixrude, L., R. J. Hemley, Y. Fei, and H. K. Mao, Thermoelasticity of silicate perovskite and magnesiowüstite and stratification of the Earth's mantle, *Science*, *257*, 1099–1101, 1992.

Turcotte, D. L., and G. Schubert, *Geodynamics*, John Wiley, New York, 1982.

Wang, Z. W., The melting of Al-bearing perovskite at the core-mantle boundary, *Phys. Earth Planet. Inter.*, *115*, 219–228, 1999.

Weidner, D. J., H. Sawamoto, and S. Sasaki, Single-crystal elastic properties of the spinel phase of $Mg_2SiO_4$, *J. Geophys. Res.*, *89*, 7852–7860, 1984.

Wiens, D. A., J. J. McGuire, and P. J. Shore, Evidence for transformational faulting from a deep double seismic zone in Tonga, *Nature*, *364*, 790–793, 1993.

Wright, K., G. D. Price, and J.-P. Poirier, High-temperature creep of the perovskites $CaTiO_3$ and $NaNbO_3$, *Phys. Earth Planet. Inter.*, *74*, 9–22, 1992.

Yeganeh-Haeri, A., D. J. Weidner, and E. Ito, Elasticity of $MgSiO_3$ in the perovskite structure, *Science*, *243*, 787–789, 1989.

Yoshioka, S., R. Daessler, and D. A. Yuen, Stress fields associated with metastable phase transitions in descending slabs and deep-focus earthquakes, *Phys. Earth Planet. Inter.*, *104*, 345–361, 1997.

Yusa, H., M. Akaogi, and E. Ito, Calorimetric study of $MgSiO_3$ garnet and pyroxene: Heat capacities, transition enthalpies, and equilibrium phase relations in $MgSiO_3$ at high pressures and temperatures, *J. Geophys. Res.*, *98*, 6453–6460, 1993.

Zerr, A., and R. Boehler, Constraints on the melting temperature of the lower mantle from high-pressure experiments on MgO and magnesiowüstite, *Nature*, *371*, 506–508, 1994.

C. W. Gable, Earth and Environmental Sciences Division, Los Alamos National Laboratory, Los Alamos, NM 87545, USA. (gable@lanl.gov)

A. Guest and G. Schubert, Department of Earth and Space Sciences, University of California, Los Angeles, 595 East Charles E. Young Drive, Los Angeles, CA 90095, USA. (alice@ess.ucla.edu; schubert@ucla.edu)